Shape Sensing of Flexible Robots based on Deep Learning

Xuan Thao Ha, Di Wu, Mouloud Ourak, Gianni Borghesan,
Jenny Dankelman, Arianna Menciassi and Emmanuel Vander Poorten

Abstract—In this paper, a deep learning method for shape sensing of continuum robots based on multi-core Fiber Bragg Grating (FBG) fiber is introduced. The proposed method, based on an Artificial Neural Network (ANN), differs from traditional approaches, where accurate shape reconstruction requires a tedious characterization of many characteristic parameters. A further limitation of traditional approaches is that they either require multiple fibers, whose location relative to the centerline must be precisely known (calibrated) or a single multi-core fiber whose position typically coincides with the neutral line. The proposed method addresses this limitation and thus allows shape sensing based on a single multi-core fiber placed off-center. This helps in miniaturizing and leaves the central channel available for other purposes. The proposed approach was compared to a recent state-of-the-art model-based shape sensing approach. A 2-DOF bench-top fluidics-driven catheter system was built to validate the proposed ANN. The proposed ANN-based shape sensing approach was evaluated on a 40 mm long steerable continuum robot in both 3D free-space and 2D constrained environments, yielding an average shape sensing error of 0.24 mm and 0.49 mm, respectively. With these results, the superiority of the proposed approach compared to the recent model-based shape sensing method was demonstrated.

I. INTRODUCTION

Advances in surgical technique have led to minimally invasive surgery (MIS) that relies on smaller incisions and typically offers less post-surgical pain and quicker recovery. Continuum and soft robots can potentially improve MIS due to their flexibility and miniature size. The application of flexible/continuum robots in MIS allows access to hard-to-reach parts of the human body and offers improved precision [1]. Many such robots for MIS have been developed in the past. In applications where *e.g.* flexible endoscopes or catheters are used, surgeons

or interventionalists require a good understanding of the input-output behaviour of these robots. Further, interventionalists wish to know in detail which space is occupied by the robot *e.g.* to judge the vicinity to critical structures or to plan adequate motion commands. Real-time knowledge of the robot's shape would greatly facilitate this task. Different methods have been proposed in the literature to model the kinematic and dynamic behaviour of soft and continuum robots. However, accurate models are complex and computationally intense [2], which limits their intra-operative use. Moreover, models are designed for a specific instrument and may require dedicated modeling efforts to characterize the input-output behaviour and the distributed shape for each individual instrument.

Different sensing modalities based on imaging (*e.g.* fluoroscopy) [3], electromagnetic (EM) tracking system [4], electrical impedance tomography (EIT) [5] or bending resistance [6] have been proposed to acquire the shape of interventional devices. Unfortunately, each sensor modality suffers from their own drawbacks. Fluoroscopic systems have the downside of emitting harmful radiation and providing only a 2D view upon the patient/instrument. Computed Tomography (CT) scan is even more harmful. EM systems do not offer uniform accuracy and are sensitive to the presence of metallic material. These problems complicate adoption in clinical practice. The use of EM and EIT for shape sensing requires different coils or electrodes to be integrated inside the structure. This can be cumbersome and may increase the size while also complicating the design of the robotic system. Gerboni *et al.* [6] integrated commercial flex bending sensors in their soft robot. While these sensors are appealing, they exhibit drift and hysteresis which requires additional modeling and identification efforts to precisely compute the bending.

In recent years, optical fibers with Fiber Bragg Gratings (FBGs) have become popular for shape sensing. Properties that make FBG optical fibers particularly attractive for integration in continuum robots are their biocompatibility, compact size, light weight, flexible nature, and safety, *e.g.* being free of the risk of electrocution. Apart from real-time knowledge of the shape, FBG fibers can also be used advantageously to characterizeand control the behaviour of soft and continuum robots. However, FBGs suffer from spectral distortion upon bending [7]. Another major challenge of FBG-based shape sensing is that strain sensing through traditional FBGs cannot distinguish strain caused by twist from strain caused by bending. Mode *et al.* [8] proposed a method to sense the 3D shape of a continuum robot incorporating bending, twisting and elongation. The method proposed by Mode *et al.* is however only verified by simulation. Further limitations to the overall estimation accuracy are due to the uncertainty in sensor location during assembly.

X.T. Ha is with the Department of Mechanical Engineering, KU Leuven, Belgium, and also with The BioRobotics Institute, Scuola Superiore Sant'Anna, Italy. (email: xuanthao.ha@kuleuven.be)

D. Wu is with the Department of Mechanical Engineering, KU Leuven, Belgium, and also with the Faculty of 3mE, TU Delft, the Netherlands. (email: di.wu@kuleuven.be)

M. Ourak and E. Vander Poorten are with the Department of Mechanical Engineering, KU Leuven, Belgium. (email: mouloud.ourak@kuleuven.be; emmanuel.vanderpoorten@kuleuven.be)

G. Borghesan is with the Department of Mechanical Engineering, KU Leuven, Belgium, and also with Flanders Make, Belgium. (email: gianni.borghesan@kuleuven.be)

J. Dankelman is with the Faculty of 3mE, TU Delft, the Netherlands. (email: J.Dankelman@tudelft.nl)

A. Menciassi is with The BioRobotics Institute, Scuola Superiore Sant'Anna, Italy. (email: arianna.menciassi@santannapisa.it)

A traditional FBG-based shape sensing method starts with measuring the wavelength shift and follows by calculating the strains at discrete locations where FBGs are inscribed. Finally, a set of curvatures and angles of the bending plane at these locations are estimated. The final shape of the robot is reconstructed by integrating curvatures and bending plane variation over the fiber length. For these traditional methods to work several characteristic parameters need to be identified carefully, such as: strain sensitive coefficients, the different distances of the outer cores to the central core, the angle of each core with respect to a reference axis (referred to as x-axis in this work) and the location of the grating. Typically, some values are provided by the optical fiber's manufacturer. However, there are three elements to consider: *(1)* these parameters may vary due to the assembly process and require thus a manual calibration. Also, as demonstrated in [9], for good performance, one may have to tackle the problem of 'intrinsic twist'. Twist may be induced during assembly when the fiber is integrated in a flexible instrument. Also this calls for a manual calibration as deviations from the true value will have an immediate and significant impact on the shape sensing performance. *(2)* Further, to sense the shape of the continuum robot, the optical fiber is normally inserted into the center channel of the continuum robot to ensure that the shape of the optical fiber follows the shape of the robot. As a result, the center channel is occupied and hence unavailable for other purposes. For some catheter designs, such as non-assembly 3D printed surgical devices [10], in which a thin central beam serves as a continuous backbone of the steering segment, it is infeasible to place a shape-sensing fiber centrally. In such case adding a central channel would excessively increase the bending stiffness of the design. Due to the aforementioned reasons, methods, where the constraint to place the shape sensing fiber centrally is not needed and where the precise location of the fiber, with respect to the centerline, could be characterized in a more automatic fashion would be highly advantageous. *(3)* Liu *et al.* [11] and Farvardin *et al.* [12] used a traditional FBG-based shape reconstruction method to estimate the shape of a 35 mm long continuum robot. In both works, when the continuum robot moves in a constrained environment, an increment in the distal tip tracking error is observed. However, shape reconstruction capability should keep its quality independent of whether or not the continuum establishes contact with the environment.

Deep learning, normally implemented based on artificial neural networks (ANNs), has drawn attention in recent years. Thanks to the ability of the ANNs to model complicated nonlinear behavior, good prediction accuracies have been reported [13]. Another strength of deep learning with respect to traditional learning methods, is that the former does not requires feature extraction procedures. Due to its advantages, a data-driven shape sensing method based on FBGs was proposed by Sefati *et al.* [14] to solve some of the problems listed above. Sefati *et al.* modeled a 1-DOF (degree-of-freedom) continuum robot introduced in [15], [16] as a pseudo-rigid body. The trained model was able to estimate the distal-end position of the robot. The robot shape is reconstructed from the distal-end estimation by solving constraint optimization for the

joint angles. One limitation of Sefati's method, which makes it difficult to extend to multi-DOF robots, is that it involves a computationally intensive optimization phase.

To address all aforementioned problems, a new data-driven approach is proposed to estimate the 3D (dimension) shape of a 2-DOF continuum robot from the measured wavelength shifts of the FBGs. A distinguishing feature of the proposed approach is that it allows data-acquisition and training when the robot moves in free space. This is simple and fast, but it generalizes well (as shown in this work) to more complex contact scenarios. The main contributions of this work are:

- for comparison, a traditional model-based shape sensing is extended for off-center fibers. A dedicated calibration method to map the curvatures measured by an off-center fiber to the centerline's curvature is introduced.
- a new data-driven ANN-based FBG auto-calibration method is introduced that estimates the curvature and the angle of the bending plane directly from measured FBG wavelength shifts, regardless of the fiber's characteristic parameters. The proposed approach makes it also possible to get accurate shape sensing capability with a single off-centered multi-core fiber, supporting miniaturization and allowing freeing up central channels for other uses.
- experiments that compare and validate both methods are conducted, the transferability of the ANN-based shape sensing method to contact situations is demonstrated. The ANN is trained in a free-space scenario, hence requiring limited training time/data, the model shows equally good shape sensing capability when the robot contacts an unknown environment.

This paper is organized as follows: Section II details the design of a 2-DOF continuum robot and the experimental setup that was built to evaluate the proposed method. Section III describes an extension of a traditional model-based shape reconstruction method. Next, the proposed auto-calibration method based on a neural network is explained in Section IV. Experimental results are shown in Section V comparing the shape sensing accuracy of the two described approaches. Section VI concludes the paper and sketches some directions for future work.

II. EXPERIMENTAL SETUP

A. Purpose-built steerable 2-DOF catheter segment

In order to collect data for training and testing auto-calibration techniques, a dedicated 2-DOF bench-top experimental setup was built (see Fig. 1). Without loss of generality, the setup features only the distal steerable segment of the envisioned active catheter. The 2-DOF of the catheter's distal segment are actuated with four embedded Pneumatic Artificial Muscles (PAMs). The catheter is fabricated out of Nitinol using metal laser cutting technology. Notches are made on the Nitinol segment so that the distal portion becomes bendable while minimally affecting compression stiffness. Since this paper aims at efficiently solving the problem of shape sensing, the design of the bendable Nitinol segment is not described here. However, details on the design can be found in [17]. The length of the flexible part (where the notches were cut)
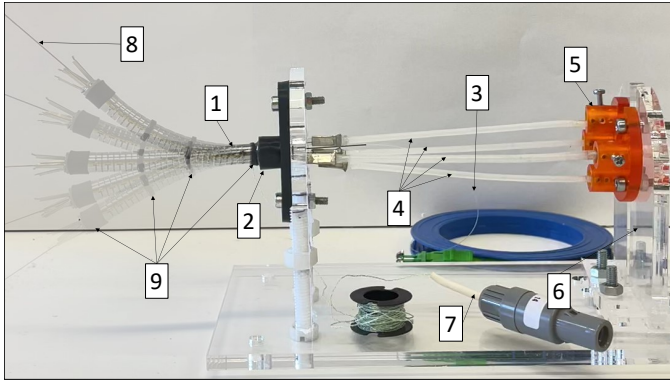
Fig. 1. A 2-DOF fluidics-driven catheter system for data acquisition and algorithm validation: 1-distal catheter segment; 2-catheter segment clamp; 3-FBG fiber; 4-Pneumatic Artificial Muscles (PAMs); 5-PAM clamp; 6-adjustable back plate; 7-EM sensor connector; 8-protective Nitinol tube; 9-heat shrink.
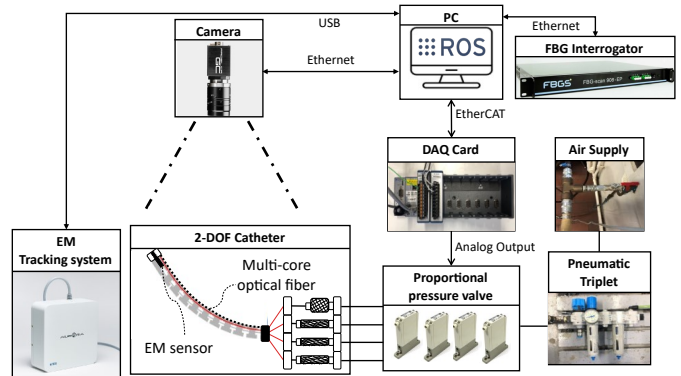

Fig. 2. Control and actuation system for the 2-DOF catheter system: A 2-DOF PAM-driven catheter segment is controlled by a set of 4 proportional pneumatic valves, which receive command signals from a PC through an NI® CompactRIO system. The PAMs are attached off-center via four steel cables to the catheter tip. When contracting they applies a bending moment to the tip. The resulting catheter tip pose is captured by an EM sensor. The FBG data and images of catheter are gathered by an FBG interrogator and a camera, respectively. A PC running ROS is used to gather sensor data.

and the diameter of the catheter are 40 mm and 6 mm, respectively. With a steerable length of 40 mm, applications in minimally invasive orthopedic [14] or ENT [18] could be envisioned. Four custom-made PAMs, which are made up of a bladder, an uninflatable tube, braids and ferrules, are used to actuate the catheter. The produced PAMs have an initial diameter of 2.1 mm and a length of 129 mm in the non-pressurized condition. The PAMs are connected off-center to the tip of the catheter by steel wires. When pressure increases, the PAM contracts and thus applies a bending moment on the catheter tip. The other end of the PAM is fixed to a movable plate, so that the pre-tension on the PAMs can be adjusted. The four PAMs are configured at an angle of 90 degrees in two antagonistic pairs, such that a 2-DOF spatial bending can be implemented. In order to accurately control the input pressure, the pressure is fed by an air supply, via a pneumatic triplet (Festo Corporation, Germany) as shown in Fig. 2. The proportional valve receives control signals from an analog output module NI-9263 (NI, Texas, USA). An EM tracking sensor (6-DOF, 0.8 mm× 9 mm, Northern Digital Inc., Ontario, Canada) is fixed to the center channel of the catheter distal tip to measure the catheter tip pose.

B. Experimental platform

To generate ground truth data for training a neural network that encodes the shape of the steerable 2-DOF catheter, an experimental platform was built as shown in Fig. 2. The setup consists of 3 modules: an interrogator (FBG-Scan 804, FBGS, Geel, Belgium) for measuring the wavelength of the distributed FBG sensors, an EM tracking system and a 2-DOF distal catheter system. To showcase that there is no need to position a shape sensing sensor centrally, a 250 micrometer four-core fiber consisting of 20 FBGs from FBGS (Geel, Belgium) is placed outside the catheter. The fiber is fixed to the catheter by means of heat shrink tubes (Fig. 2). When the catheter is at rest, the fiber was parallel to the neutral axis. During the data collection process, the FBG data was measured by the interrogator at a frequency of 200 Hz while the EM sensor poses were recorded at 40 Hz. The images from the camera

were streamed at 30 Hz. The recorded data was time-stamped and pre-processed to synchronize the FBG data with the corresponding EM sample using MATLAB (The MathWorks, Inc., Massachusetts, United States). All the experiments are carried out on a computer with an Intel 2.1 GHz core i7 processor and 32 GB of RAM, running Ubuntu 16.04. Each core contains five gratings distributed 10 mm apart from each other. Note that, each of the 20 FBG gratings has a different center wavelength. A planar NDI Aurora EM system (Northern Digital Inc., Ontario, Canada) was positioned below the steerable catheter and a monocular Prosilica camera (Allied Vision Technology, Germany) was placed approximately 30 cm above the setup. The camera faces downwards to capture the 2D shape of the catheter in the camera's image plane.

III. MODEL-BASED OFF-CENTER FIBER SHAPE RECONSTRUCTION

A new approach is proposed in Section IV that takes the wavelength shifts of four gratings at one given arc-length or cross-section as input for an ANN and directly estimates the catheter's curvature and angle of the bending plane, at this arc length. The new approach is compared to an extension of a more traditional model-based approach that is introduced in this section. Within this work, to speed up the training process, we exploit the property that during free-space motion the catheter tends to follow a constant-curvature shape [19]. An experiment, described in Section III-A, validates this constant-curvature assumption for free-space motion. From the constant curvature property, a method to estimate the shape and the angle of the bending plane from the pose of the EM sensor attached at the tip is then presented in Section III-B. In fact, due to the constant curvature assumption, the measured curvature and the angle of the bending plane should in principle be the same at each time step for all gratings, at least during the generation of training data. This knowledge is then used to speed up training. The same constant-curvature model will also be exploited as ground-truth when validating
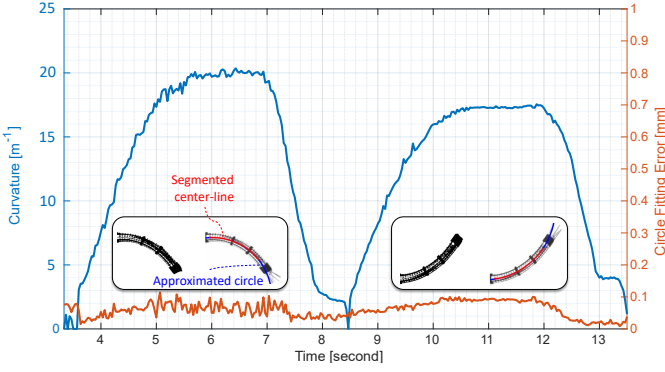
Fig. 3. Result of constant curvature verification experiment. The threshold images and the fitted circles can be seen in the inserts. The estimated curvature and errors of circle approximations are shown respectively in blue and red.
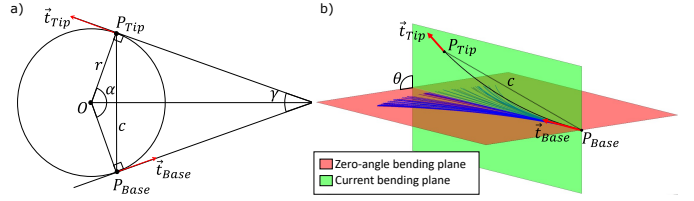

Fig. 4. Example of curvature and angle of the bending plane calculation along explanation of Section III-B: (a) curvature calculation; (b) θ is the angle between the zero-angle bending plane and the current bending plane.

shape-sensing in free-space movement. The data-collection for training and validation is described next in Section III-C.

Note that, because the multi-core fiber is not attached to the catheter's center channel, the computed set of curvatures will not reflect the real catheter curvature and hence cannot be straightforwardly used in traditional model-based shape reconstruction approaches. An additional calibration approach is presented in Section III-D that estimates the pose of each grating relative to the catheter's central line. Based upon this information the curvature information can then be mapped to the center line. From this, the 3D shape reconstruction method, described in Section III-E, can be derived. Also note that, while the proposed implementation can be considered a logic extension for anyone crafted in the art, of conventional shape reconstruction, the authors are not aware of earlier attempts to implement such model-based approach with an off-center multi-core fiber. Details on the developed ANN follow in Section IV.

A. Constant curvature model verification

To verify that the catheter follows the constant curvature model when operating in free space, the catheter was bent in a plane that is parallel to the image plane of the monocular camera. The camera was calibrated before the experiments to obtain the camera's intrinsic and extrinsic parameters using MATLAB's camera calibration toolbox [20]. The captured images are first undistorted and processed to extract the shape of the catheter in 2D by color segmentation. Each image contour is evaluated to find the contour that encloses the largest image area. The largest contour is then considered as the catheter's true contour. The contour is then skeletonized by the algorithm proposed by Lee *et al.* [21] to obtain the catheter's backbone. Since in this experiment the catheter moves in a plane that is parallel to the image plane, the 3D shape is reconstructed with a constant and known camera depth distance. The obtained set of points are then fitted with a constant curvature arc. During the experiment, different pressure values from 0 to 3.5 Bar were applied to the PAMs and the circle fitting errors were recorded. The experimental results are visualized in Fig. 3. The average circle fitting error was calculated by averaging the distance between set of points

belong to the skeleton and the approximated circle. Average circle fitting errors of 0.061 mm with standard deviation of 0.025 mm were recorded during the constant curvature model verification experiment. This low circle fitting error supports the argument to consider the free space shape as a constant curvature arc.

B. Shape and bending plane angle estimation from EM

During the ground truth generation process, the catheter is bent in free space, so the constant curvature model is valid. From the constant curvature assumption one expects that the measured curvature and the angle of the bending plane of the ground truth data are the same for all gratings. From the EM sensor, attached at the tip, the catheter tip pose can be measured. Knowing the length of the catheter and measuring the tip pose when the catheter is positioned in a straight configuration, one can calculate also the pose of the base of the steerable catheter segment. Note that the base was conveniently kept fixed during the experiment. Since the pressure values only affect the steerable portion, while other parts of the catheter were fixed, the base pose did not change during the ground truth generation process. At each configuration, the tip position P_{Tip}, the tangent vector of the tip EM sensor $\overrightarrow{t_{Tip}}$, the base position P_{Base} and the base tangent vector $\overrightarrow{t_{Base}}$ can then be used to compute the ground truth curvature and the angle of the bending plane of all points where the gratings are presented along the catheter's length. Since the constant curvature model is valid, using the tip and the base pose together with the length l of the bendable segment, as shown next, it is possible to calculate the radius r and the center O of the circle that fits the catheter's shape. The distance between the tip and the base position is equal to the chord length c. The angle between $\overrightarrow{OP_{Tip}}$ and $\overrightarrow{OP_{Base}}$ is defined as α. The relations of these parameters are depicted in Fig. 4a and given by:

$$\alpha = \pi - \gamma, \tag{1}$$

$$r = \frac{c/2}{sin(\frac{\alpha}{2})}, \tag{2}$$

where γ is the angle between $\overrightarrow{t_{Tip}}$ and $\overrightarrow{t_{Base}}$. Finally, the curvature can be obtained by

$$\kappa = \frac{1}{r}. \tag{3}$$

	70% training		30% validation	
Training data	**Dimension**	**Free-space/constrained**	**Nr. of data points**	
In-plane bending	2D	Free-space	5880	
Spiral trajectory	3D	Free-space	22858	

ANN trained and validated in free-space, while tested in both free-space and constrained space

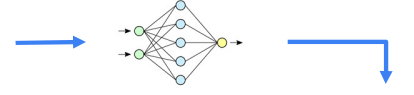| Testing manner	Dimension	Ground truth source	Testing method	Evaluation metrics
Free space validation (Section V-A)	3D	EM (with constant curvature assumption)	2 Lissajous trajectories & 2 circular trajectories	Shape reconstruction error & tip estimation error
Free space + constrained space (Section V-B)	2D (in-plane bending)	Camera (imaging segmentation)	Obstacles set at 7 different positions along the catheter	Shape reconstruction error

Fig. 5. The training, validation, and testing procedure of the MLP. The MLP was trained and validated using data collected in free space, while it was tested both in free space (introduced in Section V-A) and in a constrained space (introduced in Section V-B).

TABLE I
MATHEMATICAL FUNCTIONS OF SPIRAL (SP) USED DURING TRAINING AND VALIDATION PHASE. MATHEMATICAL FUNCTIONS OF LISSAJOUS (LI) OR CIRCULAR (CI) TRAJECTORIES (TRAJ.) IN THE TESTING PHASE. ALL UNITS ARE IN MILLIMETER.

Phase	Traj.	Mathematical functions	Traj.	Mathematical functions
Training& Validation	Sp	$x = 0.002\pi t cos(0.04\pi t)$ $y = 0.002\pi t sin(0.04\pi t)$		
Testing	Li1	$x = 0.6cos(0.04\pi t)$ $y = 0.5sin(0.08\pi t)$	Li2	$x = 0.8cos(0.04\pi t)$ $y = 0.7sin(0.08\pi t)$
	Ci1	$x = 0.4cos(0.04\pi t)$ $y = 0.4sin(0.04\pi t)$	Ci2	$x = 0.6cos(0.04\pi t)$ $y = 0.6sin(0.04\pi t)$

Different pressure values were first applied to two antagonistic PAMs to make the catheter bend in two opposite directions. The method by Torr *et al.* [22] was used to fit a plane to all tip points. This plane is defined here as the so-called *zero-angle bending plane*. The normal vector of a plane that fits the catheter shape (which is named the current bending plane) is defined by taking the cross product of $\overrightarrow{t_{Base}}$ and $\overrightarrow{t_{Tip}}$. At each configuration, the angle of the bending plane θ is determined as the angle between the normal vectors of the zero-angle and the current bending plane. An example of the bending plane angle calculation can be seen in Fig. 4b. The blue lines show the catheter shape during the process of deriving the zero-angle bending plane while the black line shows an arbitrary current configuration of the catheter.

C. Data collection

To create the training data, two antagonistic PAMs were first pressurized sequentially to generate the zero-angle bending plane as described in Section III-B. The catheter was then controlled to follow a 3D spiral trajectory (described in Table I) that broadly cover the work space of the steerable catheter and that starts from the straight configuration. The training and validation data comprises 5880 samples from zero-angle bending plane and 22858 samples from the spiral trajectory, leading to a total of 28738 data points. The maximum curvature that was recorded during training was 19.3 m⁻¹. The 70% of collected data sets were used to train the ANN, while the rest 30% were used to validate the ANN. This was a random split. It was conducted using the 'train_test_split' function in the 'scikit-learn', an open source machine learning library. The information on the training data is summarized in Fig. 5.

The proposed approach was tested with EM ground truth and image ground truth. Free space test sets with EM ground truth were created to verify the proposed approach by controlling the catheter's distal-tip to follow two circular and two lissajous trajectories. Note that the test trajectories are independent data sets that have completely different patterns with respect to the training set. By doing so, leakage from the training to the test set is avoided ensuring a proper validation of the approach. The mathematical function of trajectories are summarized in Table I. Since the catheter was controlled in free space, the constant curvature assumption together with tip and base pose were used to generate the ground truth shape. However, as mentioned above, the constant curvature assumption is not valid in a constrained environment. To test the performance of the ANN in a constrained space, the ground truth shape of the catheter was generated from camera images instead of using the catheter tip and base poses. The catheter was bent in a plane that is parallel to the camera both in free and a constrained environment. During constrained environment testing, obstacles were fixed at different places along the catheter length. These obstacles caused the catheter to deform into non-constant curvature shapes.

D. Model-based off-center fiber calibration

By using a conventional model-based approach, a set of curvature κ_f and angle of the bending plane θ at discrete points along the fiber where the FBGs are inscribed can be calculated based on the fiber core's geometry [23]. However, since the multi-core fiber is not placed on the central axis of the catheter, the calculated curvature does not indicate the catheter's curvature. The relation of the calculated curvature κ_f and the catheter's curvature κ is given by:

$$\kappa = g(\kappa_f) = \left(\kappa_f^{-1} - \frac{\overrightarrow{OO'_f} \cdot \overrightarrow{OK}}{||\overrightarrow{OK}||} \right)^{-1}, \qquad (4)$$

where O'_f is the projection of O_f (center of the fiber) on the bending direction vector $\overrightarrow{OK}$. The relative position of the multi-core fiber O_f and the center-line of the catheter O is characterized by the distance to the center-line d_f and the
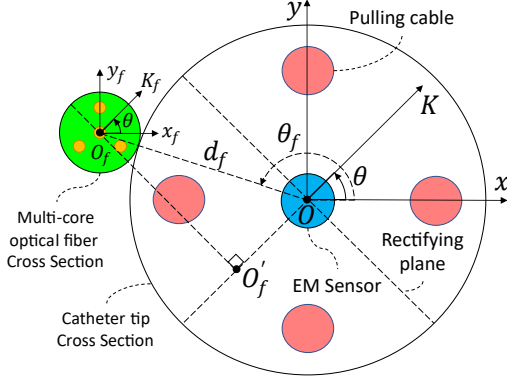
Fig. 6. Cross sectional view of the catheter tip and the multi-core FBG fiber where θ is the angle of the bending plane with respect to the x_c-axis, d_f is the distance between the center of the catheter and the fiber's central axis, and θ_f is the angle between x-axis and the center of the fiber O_f.
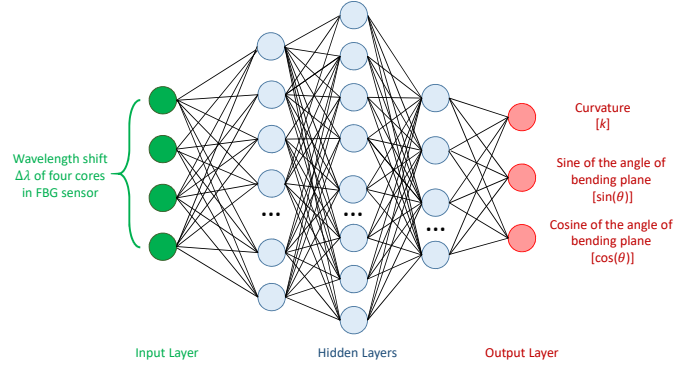

Fig. 7. A multilayer perceptron (MLP) for FBG calibration. The four wavelength shifts $\Delta\lambda$ from the four-core FBG fibers are entered into the input layer of the proposed MLP. The output layer has three neurons. One neuron predicts the curvature, while the other two predict the sine and the cosine of the angle of the bending plane. Five of these MLPs are established for the five gratings that are distributed over the entire length of the catheter segment.

angle θ_f between $\overrightarrow{OO_f}$ and the x-axis. A cross sectional view of the multicore-fiber and the catheter tip is shown in Fig. 6.

An optimization problem is formulated to find d_f and θ_f by minimizing the following objective cost function

$$\underset{d_f, \theta_f}{\mathrm{argmin}} \frac{1}{n \times m} \sum_{i=1}^{n} \sum_{j=1}^{m} ||g(\kappa_{fi,j}) - \kappa_{gt_i}||, \qquad (5)$$

where m is the number of points where FBGs are inscribed along the optical fiber length, n is the number of samples in the training data and κ_{gt_i} is the ground truth curvature that is generated from EM poses. Two algorithms supported by MATLAB, namely *trust-region reflective* [24] and *Levenberg-Marquardt* [25] were used to solve the optimization problem. The result of *trust-region reflective* was chosen since it yields lower value for the objective function (approximately 15%).

E. Shape reconstruction

As explained in the following, the discrete estimated curvature of the catheter's central axis and the angle of the bending plane are interpolated. This ensures the continuity of the estimated curvature and improves the shape reconstruction accuracy. The catheter shape is represented as a space curve, which can be described as a set of curvature $\kappa(s)$ and torsion $\tau(s)$, where s is the variable arc length. The torsion $\tau(s)$ is the rate of change of angle of the bending plane with respect to the arc length. Curvature and torsion profiles determine the evolution of the tangent $\overrightarrow{t}$, the normal $\overrightarrow{n}$, and the binormal $\overrightarrow{b}$ unit vectors along the length of the catheter. By solving the differential Frenet-Serret formulae, the evolution of the TNB frame is obtained [26]. The Cartesian position of each point that belongs to the catheter length $C(s)$ follows then by integrating

$$C(s) = \int_{0}^{s} \overrightarrow{t} \, ds. \qquad (6)$$

In this work, (6) is solved by using Helical Extension Method (HEM) [27] as suggested in [9].

IV. ANN-BASED OFF-CENTER FIBER SHAPE RECONSTRUCTION

A. Design of the ANN

In this work, a multilayer perceptron (MLP) is used to auto-calibrate the shape sensing functionality of the robot. A multilayer perceptron is a class of feed forward artificial neural network that consists out of an input layer, several hidden layers and an output layer [28]. Except for the neurons in the input layer, each neuron adopts a nonlinear activation function. These nonlinear activation functions turn the MLP into a nonlinear perception, thus distinguishing itself from linear approaches, such as linear regression. Thanks to a large number of neurons and the possibility to make use of multiple types of nonlinear activation functions, MLPs can model complex nonlinear behavior [29]. The training of the MLP is based on a supervised learning algorithm called back-propagation [30]. The training procedure requires sufficient data containing various patterns. The MLPs developed here relate the measured wavelength shifts from FBGs directly to the curvature and angle of the catheter's bending plane without explicit knowledge of the correspondence between the fiber's position and the catheter center-line or explicit knowledge of the characteristic parameters of the fiber. Note that the reason for using wavelength shifts $\Delta\lambda$, instead of raw wavelengths values, is that the absolute value of the wavelength itself could be influenced by environmental factors such as temperature and humidity, which is less for the case of wavelength shifts.

The length of the flexible part of the catheter segment is 40 mm. Since the distance between neighbouring gratings is 10 mm, only five sets of curvature and angle of the bending plane is needed to reconstruct the shape. Therefore, five MLPs, as shown in Fig. 7, were employed. Here, rather than a large MLP that takes five gratings together, five separate MLPs were trained. This allows efficient training and helps transferability of the results to more general scenarios. Training can be done in free space only (which is faster than training every

possible contact situation), but - as demonstrated in this work - still allows learning the behavior/parameters of each separate grating. This is found helpful to generalize to more general cases where the shape deviates from a single constant curvature for all the five gratings (as would be expected in free space).

Each MLP automatically interprets the strains from the four gratings of an individual location. Each MLP (see Fig. 7) consists of five layers i.e. one input layer, three hidden layers and an output layer. The input layer has four neurons, which receive the wavelength shifts $\Delta\lambda$ that are collected from a four-core FBG fiber. The catheter was first placed in a straight configuration to measure the unstrained Bragg wavelength λ_0 of each grating. The wavelength shifts were then calculated as:

$$\Delta\lambda = \lambda - \lambda_0, \tag{7}$$

where λ is the strained Bragg wavelength.

B. Hyperparameter tuning of the ANN

The first, second and third hidden layer have 180, 360, and 90 neurons, respectively. The number of neurons in the different hidden layers have been derived through a hyperparameter tuning procedure that was conducted on the 3rd set of gratings. As shown in Table II, different numbers of hidden layers ranging from 1 to 4 layers with different combinations of neurons in each layer were tested. At each configuration, the MLP was trained for three times. An average of the validation losses of the last 20% epochs (namely for 350 epochs, the average of $350 \times 20\% = 70$ validation loss values) was recorded as the average validation losses, as shown in Table II. The standard deviations among the three trials are also indicated, right after the average validation losses in Table II, for better comparison. By checking the result among multiple training sessions (in this case 3) and by averaging also the validation losses over epochs, the chance for an accidental outcome/error is reduced. Validation loss, namely the summation of the Mean Squared Error (MSE) of the three outputs with respect to their ground truth, is used during the validation phase. After multiplying with a scale factor = 1 [mm], the curvature output becomes unitless. Because the sine and cosine of the bending angle are also unitless, the validation loss, which is a summation of three unitless values, has no unit and immediate physical meaning. The training time is listed as well. Computations were done with a 4 GB NVIDIA® Quadro CUDA-capable GPU. The combination of 180-360-90 produced the lowest average validation loss (0.0057), thus this configuration was chosen for the final MLP structure. The influence of the batch size was also tested and is visible in the last row of Table II. The best performance of 180-360-90 was based on a batch size of 16. The results showed that increasing the batch size to 32 did not improve the performance (validation error rises from 0.057 to 0.063), while decreasing the batch size to 8 not only leads to a larger validation error, but also significantly raises the training time from 2.02s to 4.21s per epoch.

A Rectified Linear Unit (ReLU) is used as the activation function and added after each hidden layer. The output layer has three neurons. One of the outputs is the curvature. The two
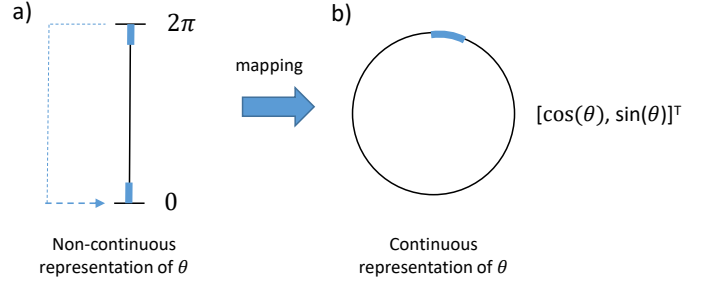

Fig. 8. Instead of directly estimating the angle of the bending plane, the proposed MLP divides it into two outputs, i.e. the sine and cosine of the angle of the bending plane. This approach transforms the discontinuous rotation representation *(left)* into a continuous representation *(right)*, thus facilitating the fitting of the neural network.
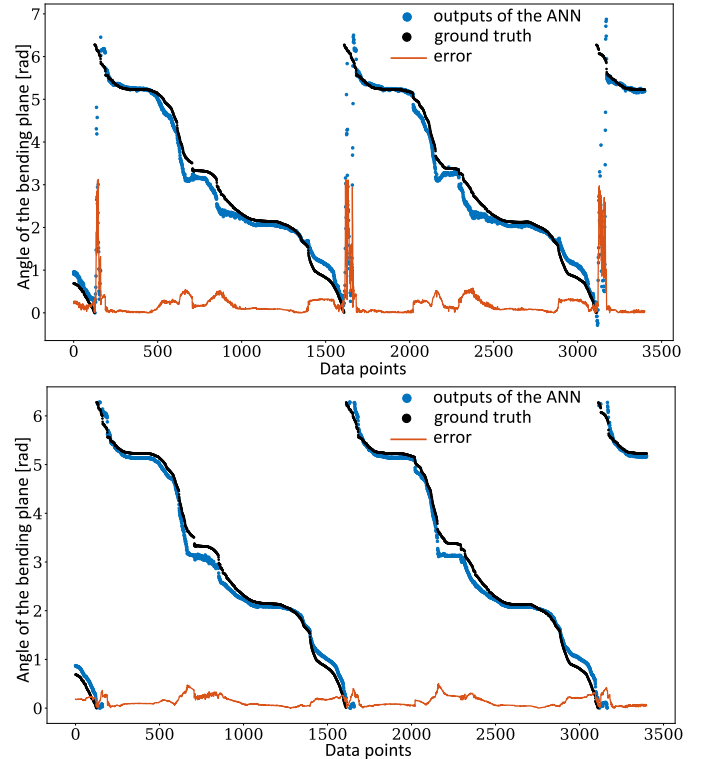

Fig. 9. Prediction of the angle of the bending plane of grating 3 using different representation methods: (a) non-continuous representation: as can be seen in the dashed green boxes, the MLP with the non-continuous representation generates large errors in the transition region $[0,2\pi]$; (b) continuous representation: MLP performs well in the transition region, thus produces small errors.

other neurons predict the sine and the cosine of the angle of the bending plane. This allows circumventing the discontinuity of the angle at 0 and 2π (Fig. 8a) that is otherwise difficult to cope with for an ANN [31]. The prediction results of the MLP are shown in Fig. 9a for the case where the non-continuous representation has been used. As visible in the green dashed boxes, there are many haphazard points distributed over the transition region $[0, 2\pi]$. The error plot (in green) in this region generates a peak, where the error is significantly larger than the other regions. In this case, the Mean of Absolute Error (MAE) of the 3rd set of gratings is 0.21 rad. If we reconfigure and train the ANN with its output to the sine and cosine of the

TABLE II
HYPERPARAMETER TUNING OF MLP STRUCTURE

Number of hidden layers or batch size	Hidden size	Avg. validation loss (std)	Training time per epoch (s)
1	360	0.0097 (0.0006)	1.42
	720	0.0092 (0.0002)	1.43
2	30-15	0.0078 (0.0004)	1.71
	90-45	0.0068 (0.0004)	1.70
	180-90	0.0067 (0.0002)	1.75
	360-180	0.0066 (0.0002)	1.83
	480-240	0.0067 (0.0002)	1.77
3	30-60-15	0.0071 (0.0006)	1.98
	60-120-30	0.0067 (0.0005)	2.01
	180-240-90	0.0068 (0.0004)	2.03
	180-360-90	**0.0057** (0.0003)	2.02
	180-360-180	0.0065 (0.0001)	2.09
	360-720-180	0.0060 (0.0003)	2.21
4	60-120-120-30	0.0064 (0.0003)	2.20
	60-180-360-90	0.0064 (0.0002)	2.31
	90-180-360-30	0.0066 (0.0003)	2.30
	180-360-360-90	0.0066 (0.0002)	2.34
Batch size = 8	180-360-90	0.0061 (0.0002)	4.21
Batch size = 32	180-360-90	0.0063 (0.0002)	2.02

TABLE III
FEATURE ABLATION STUDY

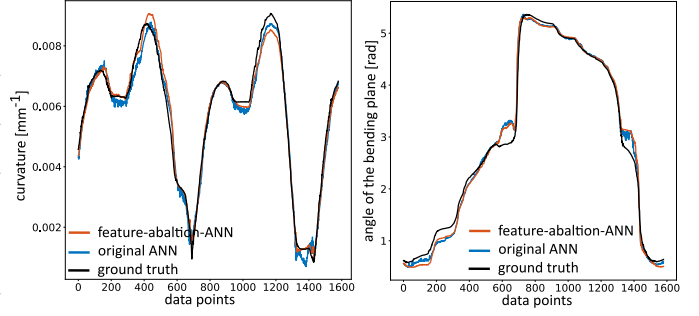|	Avg. validation loss (std)	Percentage increase
remove the 1st core	0.0065 (0.0004)	14.0%
remove the 2nd core	0.0081 (0.0003)	42.1%
remove the 3rd core	0.0079 (0.0006)	38.6%
remove the 4th core	0.0069 (0.0001)	21.1%

Fig. 10. The results of the feature ablation study. The feature-ablation-ANN (with three inputs) and the original ANN (with four inputs) trained for grating set 3 were evaluated on testing trajectories lissajous (1). The feature-ablation-ANN could achieve a comparable performance as the original ANN even if the information from the central core is not provided.

angle of the bending plane, the rotation is represented in a continuous fashion (Fig. 8b). This will improve the learning efficiency of the MLP (see Fig. 9b). The MAE obtained in this case (results shown in Fig. 8b) is 0.13 rad, which is 38.1% better than the non-continuous representation. The angle of the bending plane can be finally calculated by wrapping the angle back to the interval of 0 to 2π via the operation:

$$\theta = atan2(\frac{sin\theta}{cos\theta}). \tag{8}$$

To increase the learning efficacy, all the input and output training data were normalized between [-1,1] following (9).

$$x_{norm} = (b - a)\frac{x - x_{min}}{x_{max} - x_{min}} + a, a = -1, b = 1. \tag{9}$$

The output normalization regulates the three outputs to the same range, thus the ANN learns the three outputs with equal efforts. Here, a normalization is carried out instead of a standardization because normalization is suitable for use when the distribution of data does not follow a Gaussian distribution. In addition, ANN is an algorithm that does not assume/prerequire any type of data distribution. Note that in (9), the variable x represents respectively the wavelength shift $\Delta\lambda$, curvature κ, and the sine and the cosine of the angle of the bending plane: $sin(\theta)$ and $cos(\theta)$, respectively.

C. Feature ablation study of the ANN

Apart from hyperparameter tuning, a feature ablation study was conducted to determine the contribution of each input feature to the overall performance of the ANN. Ablations were carried out by removing one of the four inputs. This means

that the ANN used for the feature ablation study (hereinafter referred to as "feature-ablation-ANN") only has three inputs. Next, the feature-ablation-ANN was re-trained. To investigate the effect of the ablation, the performance of the feature-ablation-ANN was first evaluated on the validation set. The validation losses are reported in Table III-E. It shows that removing the first core (central core) leads to the lowest increase (14.0%) in validation loss. Because, the central core practically coincides with the fiber's neutral axis, it is not sensitive to bending strain. Therefore, it provides less information to the ANN compared to other cores and removing it has not that large impact.

The feature-ablation-ANN (with central core removed) was further validated on the test set. An ANN was trained for each grating. Five feature-ablation-ANNs are applied to the four testing trajectories (see Table II). The errors of curvature and the angle of the bending plane generated by the feature-ablation-ANN were compared to that of the original ANN. One group of results tested on the trajectory Lissajous (1) is shown in Fig. 10. The results show that the average curvature error of the feature-ablation-ANN (0.56 m^{-1}) is slightly smaller than the original ANN (0.62 m^{-1}). Their average errors of the angle of the bending angle are comparable, namely 0.20 rads for feature-ablation-ANN and 0.21 rads for original ANN. This can be explained by the fact that the central core provides redundant information. The ANN could achieve better performance when the redundant input information is removed. However, it is expected that the information from the central core could be beneficial in more complex loading cases such as a longitudinal load, and/or a variable temperature. These disturbances have not been tested at this point and remain the subject of further work. Based on this consideration, this work continues with the original ANN. Note that the aim of the hyperparameter tuning procedure of Section IV-B and the feature ablation study described here is to find efficient combinations of hyperparameters and ANN structures. The aim is not to find the optimal configuration for a certain data-set, as this would not necessarily guarantee optimal performance on other datasets.

D. Summary of hyperparameter study

TABLE IV
HYPERPARAMETERS FOR THE MLP

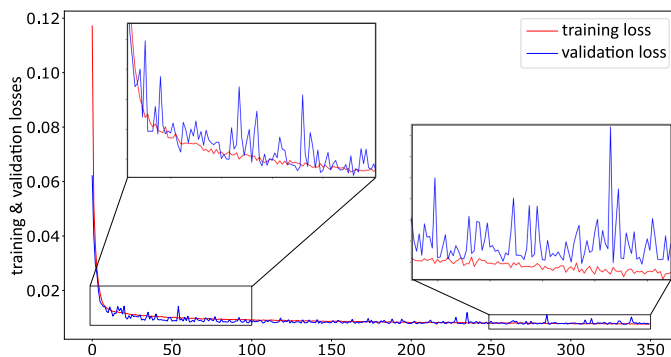|	Number of hidden layers	Number of neurons per cell	Activation functions	Optimizer	Loss function	Training-subset /Validation ratio	Batch size	Learning Rate	Epochs
MLP	3	180, 360, 90	ReLu	Adam	L2 Loss	70% 30%	16	10^{-5}	350

Fig. 11. Loss trend (grating 3) presented as training loss (red) and validation loss (blue) vs. the number of epochs.

The hyperparameters of each MLP are listed in Table IV. Hyperparameters, e.g. number of layers and number of neurons per layer, were chosen through a thorough hyperparameter tuning procedure (see Table III). Other hyperparameters, e.g. Adam optimizer [14], training/validation ratio 30%/70% [32], [33], or ReLu activation function [14], were selected based on previous research or empirically. The network was implemented using Python, and in particular PyTorch, an open source machine learning library. Ubuntu 20.04 was the operating system that was used. Each MLP has been trained for 350 epochs until the training and validation loss reached a plateau. The whole training time was less than 15 minutes. The loss trend of one training session was shown in Fig. 11. The training results indicate that the MLP converged at the end of the training process. The average inference time of the MLP for a single output is around 0.18 ms. Also considering the MLP has a practical structure among the ANNs, it is feasible for the users to train an MLP in a short time. The users can employ the trained MLP to achieve the calibration of the FBG as well as the reconstruction of the robot shape real-time.

V. RESULTS AND DISCUSSION

Figure 5 summarizes the performance of the trained MLP. The MLP was first verified in free space by reconstructing the shape of the robot while it was controlled to follow two Lissajous and two circular trajectories. Subsequently, verification in a constrained space took place. Here, the catheter was brought into contact with an obstacle at different locations along its length.

A. Free space experiments with ground truth generated EM

In the free space experiment, with ground truth generated by the EM, the catheter was commanded (in open loop) to roughly follow the predefined trajectories as shown in Table I. The catheter bends with curvatures up to 15 m^{-1}. Note that no effort was done to follow the said trajectories closely (*i.e.*,

open loop control was implemented) as this work focuses on predicting reliably the catheter shape, not on closely following a trajectory. The ground truth of these experiments was generated using the tip and base poses together with the constant curvature assumption of the catheter. The error as function of the arc length is defined as the Euclidean distance between the reconstructed and the ground truth data:

$$E_{dist} = d_{min}(S_{gt}, S_{est}), \tag{10}$$

where S_{est} is the reconstructed shape expressed as a set of k points $S_{est} = [s_1 s_2 ... s_k]$ and $s_{i \in \{1,...,k\}}$ is the 3D coordinate of each point. The distance error E_{dist} is the distance between the ith point of the estimated shape S_{est} to the closest point on the ground truth shape S_{gt}.

The blue lines, which are shown in the graphs in the first row of Fig. 12a-d, depict the estimated catheter shapes using the ANN approach. The distance errors are shown in color-coded map graphs in the second row of Fig. 12 in panels e-h. The histograms showing the mean and the max error are shown in Fig. 12i-f. The mean error for one shape is calculated by averaging the E_{dist} while the max error shows the largest value in E_{dist} at each time step. The free space experimental results with EM ground truth are shown in the first part of Table V. In this table, the mean and max error for each shape at a single time step using our proposed ANN approach and the traditional model-based approach are reported with their standard deviation. The overall max error which shows the largest error in each experiment is also mentioned in Table V. One can observe that the proposed approach can estimate the catheter shape with good accuracy with an overall mean and max reconstruction error of 0.244 mm and 0.639 mm, respectively. The color-coded map graphs (Fig. 12e-h) show that the maximum error typically appears at the tip of the catheter. This is logical as the errors are integrated along the catheter length, and therefore the maximum error can be considered as the estimated tip error. The catheter experienced different bending in the four different trajectories. The largest mean error of 0.309 mm appears at the circular trajectory (2) where also the largest curvature takes place. The overall maximum errors of the two Lissajous trajectories were 1.080 mm and 1.009 mm, while the maximum errors of the two circular trajectories were 1.773 mm and 1.795 mm.

Figure 13 shows the mean error over the time of Lissajous (1) experiment together with the estimated angles of the bending plane for each grating and the ground truth angles of the bending plane. The mean error increases at the transition points of the angle bending plane while the catheter crosses the zero-angle of the bending plane (marked with dashed squares in Fig. 13). Note that here the zero-angle of the bending plane is calibrated to be aligned with the switching point of the two antagonistic muscles (Fig. 6) of the catheter. The large error at
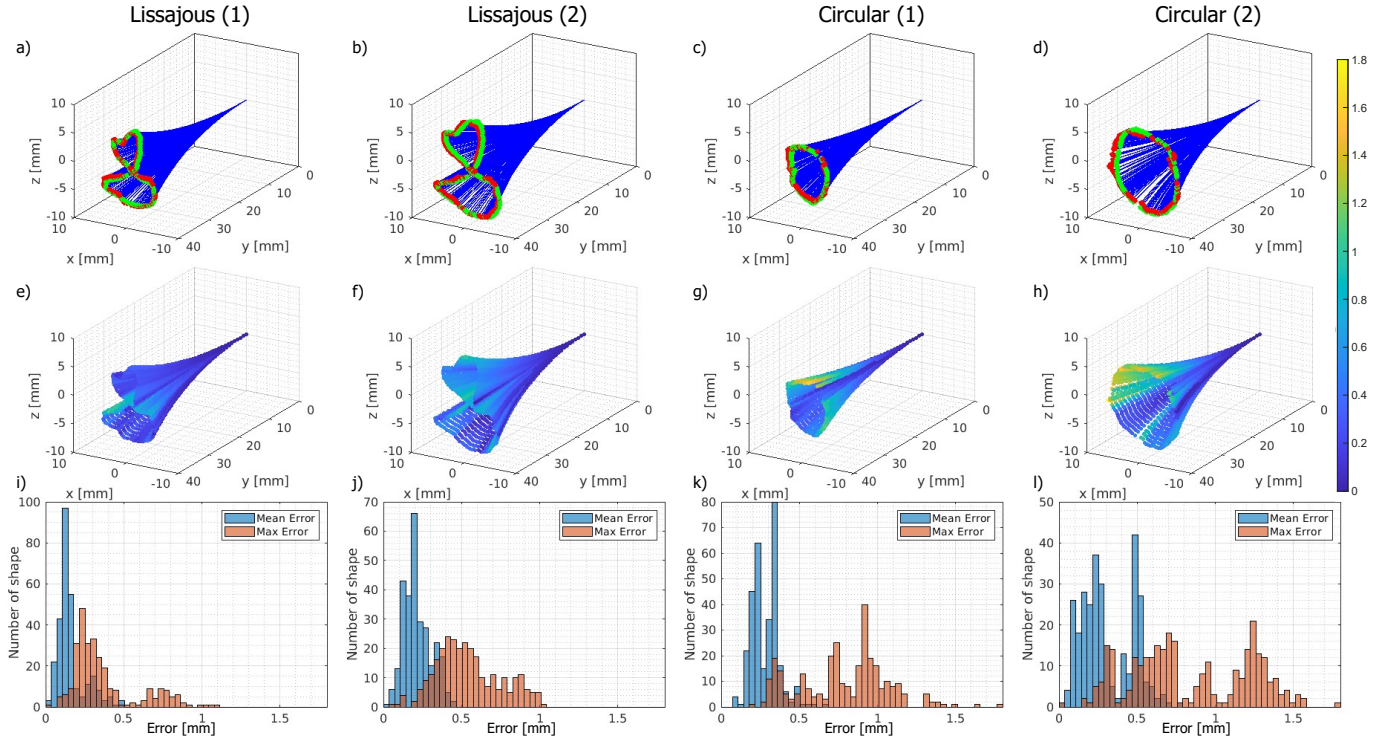
Fig. 12. The results of free space shape sensing experiments with EM ground truth using ANN approach: (a)(e)(i) lissajous (1); (b)(f)(j) lissajous (2); (c)(g)(k) circular (1); (d)(h)(i) circular (2). The catheter reconstructed shapes are presented by blue lines in the graphs displayed on the first row while the images on the second row show the color-coded Euclidean distance errors of each point along the catheter length. The images on the third row show the histogram of the mean and max error for each trajectory.

TABLE V
EXPERIMENTAL RESULTS FOR ANN AND MODEL-BASED APPROACH IN FREE SPACE, GROUND TRUTH GENERATED BY EM (FIRST FOUR ROWS), AND CONSTRAINED ENVIRONMENT, GROUND TRUTH FROM CAMERA (LAST SEVEN ROWS). THE INDIVIDUAL ERROR FOR EACH CONSTRAINED EXPERIMENT FIG.14(B)-(G) ARE ALSO REPORTED.

| Experiment		Mean error for one shape at a single time step (mm)		Max error for one shape at a single time step (mm)		Overall max error (across all shapes) (mm)	
		ANN	Model	ANN	Model	ANN	Model
EM ground truth	lissajous (1)	0.158 ± 0.090	0.250 ± 0.130	0.370 ± 0.213	0.746 ± 0.372	1.080	1.562
	lissajous (2)	0.216 ± 0.088	0.304 ± 0.160	0.542 ± 0.205	0.882 ± 0.503	1.009	1.644
	circular (1)	0.285 ± 0.086	0.352 ± 0.259	0.782 ± 0.282	1.038 ± 0.789	1.773	2.148
	circular (2)	0.309 ± 0.165	0.335 ± 0.156	0.838 ± 0.380	0.945 ± 0.497	1.795	3.007
Camera ground truth	(a)	0.491 ± 0.053	0.569 ± 0.151	0.624 ± 0.096	0.721 ± 0.203	0.851	1.170
	(b)	0.507 ± 0.048	0.621 ± 0.039	0.711 ± 0.055	0.572 ± 0.171	0.839	0.926
	(c)	0.460 ± 0.028	0.641 ± 0.039	0.708 ± 0.073	0.859 ± 0.071	0.816	0.938
	(d)	0.503 ± 0.021	0.565 ± 0.029	0.665 ± 0.038	0.761 ± 0.052	0.756	0.819
	(e)	0.483 ± 0.018	0.405 ± 0.133	0.632 ± 0.027	0.533 ± 0.161	0.658	0.723
	(f)	0.499 ± 0.016	0.510 ± 0.016	0.603 ± 0.040	0.627 ± 0.027	0.675	0.678
	(g)	0.511 ± 0.021	0.654 ± 0.024	0.701 ± 0.037	0.778 ± 0.039	0.800	0.848
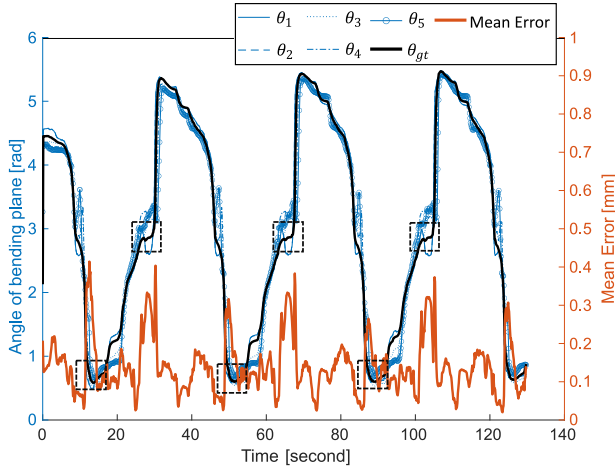
Fig. 13. The estimated angles of the bending plane of each grating (blue), ground truth angle of the bending plane (black) and mean error (orange) of lissajous (1) experiment are plotted over the time. The transition regions where there are increases in mean error are marked with dashed square.

the transition point is due to the fact that the low frequency of the EM sensing is not able to capture fast dynamic movement of the catheter tip when it crosses the switching points of the two antagonistic muscles. The unavoidable non-linearities (e.g. hysteresis, dead zone) make the catheter tip movement more unpredictable. This can be clearly seen in Fig. 9. Consequently, the quality of the training data gathered at the transition point is worse. In turn, this leads to lower accuracy, here seen as a larger error of the bending plane angle around the zero-angle bending plane.

For comparison, the catheter shape was also reconstructed with a conventional model-based shape sensing method introduced in [23] with the calibration step described in Section III-D. The mean and maximum reconstruction errors achieved by this conventional method are 0.311 mm and 0.906 mm, respectively, which are 21.5% and 29.5% larger than the results achieved by the ANN-based method (Fig. 14h).

B. Free space and constrained space experiments with ground truth generated by the camera

In the experiments with ground truth generated by the camera, two antagonistic PAMs were actuated successively to make the catheter bend in a plane parallel to the camera's plane. This allows us to use the camera as a source for ground truth generation. To generate the constrained environment test sets, rigid obstacles were fixed at various locations along the catheter length as shown in Fig. 14. During these experiments, the PAMs were pressurized with a maximum value of 3.5 bar which results in the maximum recorded curvature of 20 m^{-1}. Given the short length of the bendable segment (approximately 40 mm) and the large size of vessels where we are targeting at, the segment would only assume to get into S-shape configuration when an intense contact appears at the tip. Such contact would need to be maximally avoided. For these reasons, we did not include S-shaped bending while evaluating our proposed approach.

By controlling the catheter to move in the image plane, the camera was able to capture the entire shape of the catheter. The images recorded by the camera were used to generate the ground truth for the unconstrained and the constrained environment experiments since the presences of extrinsic disturbance (obstacles) make the catheter deform into shapes for which the constant curvature assumption is no longer valid. The interaction with an obstruction complicates the catheter shape segmentation process. To address this issue, the heat shrink's positions along the catheter length were tracked rather than the centerline of the entire catheter. Color segmentation was first applied to the input image to identify the contours of the heat shrink. The heat shrinks' locations in the image frame $P_{m \times 2}^{Img}$ (where m is the number of heat shrink) were then determined by the center of the recognized contours. Since the center points of the heat shrinks were moving in a plane during the experiments, the 2D positions of these points can be converted to 3D positions by adding a fixed z-value (i.e. $z = 0$). The 3D positions of the heat shrinks in the ground truth frame were defined as $P_{m \times 3}^{GT} = scale \times [P_{m \times 2}^{Img} \; 0_{m \times 1}]$ where $scale$ is a camera scale factor calibrated by observing a known-size chess board. To register the FBG shape reconstruction frame and the ground truth frame, a spatial calibration step as detailed in [23], was done to find the correspondence between the measured shape and the measured positions of the four heat shrinks. The catheter was fixed at the base and was bent in two configurations symmetric with respect to the straight configuration. The distance between the first and second configuration of each corresponding point at a given arc length along the reconstructed shape was measured. The travel distance of each point along the length of the reconstructed shape was then compared to the travel distance of each heat shrink to find the corresponding arc length of each heat shrink. An example of this spatial calibration process is shown in Fig. 15.

To localize the 3D reconstructed shape in the ground truth frame, m shape points in the FBG shape reconstruction frame together with their corresponding points in the ground truth frame ($P_{m \times 3}^{GT}$) are used to find a rigid transformation matrix at each time step. In this work, a point-to-point registration method proposed by Horn [34] was used. To compare the efficiency of the ANN-based and the model-based approach, the mean and the maximum distance between the 4 heat shrink points and their corresponding points in the estimated shape in the ground truth coordinate frame were calculated.

Figure 14a shows the estimated shape in the unconstrained experiments while Fig. 14b-g visualizes the catheter shape in the constrained environments. The experimental results of the free space and of the different contact location experiments, with camera ground truth, are summarized in the second and third part of Table V. The quantitative shape reconstruction results using the ANN and the model-based approach are shown in Fig. 14h. The mean, maximum value and the standard deviation of the shape reconstruction error are plotted in the constrained environment with EM ground truth, free environment and constrained environment with camera ground truth. It can be observed that the proposed ANN approach yields a mean shape deviation of 0.491 mm and 0.497 mm
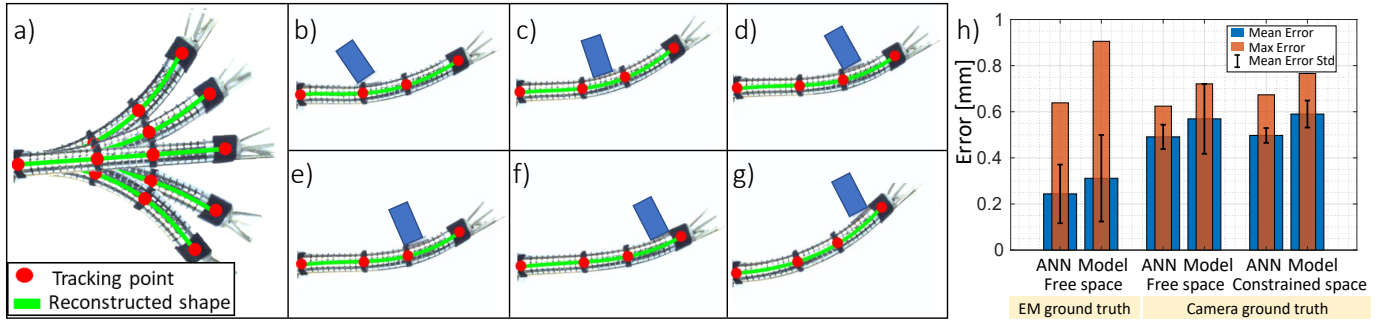
Fig. 14. The results of constrained environment shape sensing experiments using the ANN approach: (a) free space; (b)-(g) constrained space. The catheter reconstructed shapes are presented by a green line while the tracked makers are shown in red. The quantitative shape reconstruction results of the experiments with EM ground truth and with camera ground truth using ANN and model-dependent approach are presented in (h).
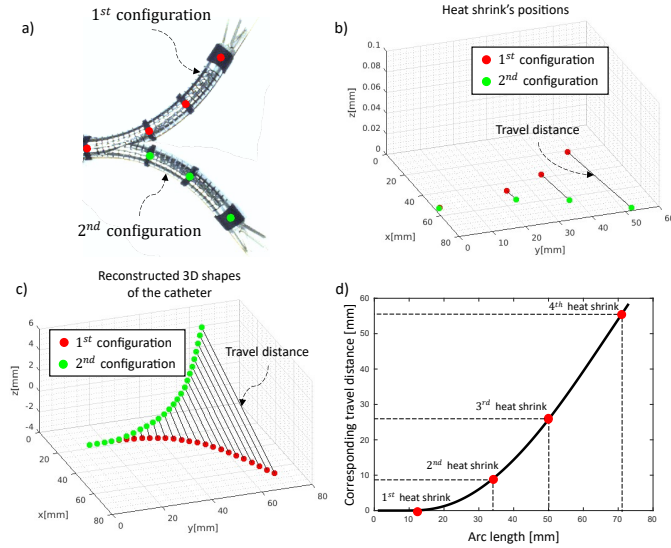

Fig. 15. The spatial calibration step to find the correspondence between the heat shrinks position and the 3D reconstructed shape. Catheter was first bent in two configurations as shown in (a). The heat shrink's positions were then extracted by image processing and transform to the ground truth coordinate frame as can be seen in (b). The 3D shapes of the catheter in two configurations were reconstructed in the FBG coordinate frame (c). The travel distance between two configurations of each point along the catheter length was calculated and compared to the travel distance of each heat shrink to find the correspondence (d).

in the free and constrained environment experiments with camera ground truth, respectively (Fig. 14h). The traditional model-based approach shows a similar consistent accuracy of approximately (0.568 mm) in both free space and constrained space experiments. In terms of the maximum reconstruction error, the ANN improved the performance over the traditional approach by 13.9% and 11.8% in free space and constrained space, respectively.

C. Discussion

Referring to Fig. 14h, one can note that the maximum error in the free space experiment with EM ground truth is larger than the maximum error of the experiments with camera ground truth. This is due to the fact that the evaluation metrics in the EM ground truth experiments (pointwise shape reconstruction error over the entire length) are different from

those used in the camera ground truth experiment (shape reconstruction error using four heat shrinks as reference points). Therefore, the error between these two experiments represents two different metrics and are not comparable. These experimental results reflect the superiority of the proposed ANN approach compared to the traditional model-based approach in all the three experiments. It is worth to mention that thanks to the fast response and the high frequency streaming rate of the FBGs, the shape reconstruction algorithm runs at 200 Hz using MATLAB on a computer with specifications mentioned in Section III-C.

Considering the average error and the maximum shape sensing error, the authors believe, at their best knowledge, that this method outperforms other results reported in the literature. In addition, our method only requires data acquisition in free space to train the ANN, and the trained ANN can be generalized to the constrained space as well. The ANN efficiently learns the mapping from the wavelength shift $\Delta\lambda$ to the curvature and the angle of the bending plane. This mapping is in fact an intrinsic property of the robot. Indeed it is shown through these experiments that this mapping does not depend on whether the robot is in contact with obstacles or not. Hence it can be said that the ANN model trained in free space is well transferable to contact situations. Aside from the elegance and knowledge that free space training suffices, the training itself is, with 30 minutes training in total, also very fast. One would expect this training time to rise proportionally for longer sections, but training would only be required once, e.g. right after construction of the catheter.

In addition, considering the concerns arising from the black-box nature of DL methods, two precautions are proposed in case the ANN fails: 1) the maximum curvature that can be achieved by the flexible robot is identified before the interventions. If the ANN prediction is greater than this threshold, or less than zero, then the system should indicate to the clinicians that the reconstructed shape is unreliable; 2) the traditional model-based approach that is used as a comparison to the ANN will be used in parallel with the ANN. If the situation described in 1) occurs, or the difference between the model-based approach and the ANN is too large, or if the ANN has no outputs at all, then the system switches to the traditional model-based approach for shape reconstruction. This mechanism takes advantage of the superior accuracy

of the ANN, but at the same time offers redundancy to mitigate the risks when the ANN approach would fail during interventions.

VI. Conclusion and Future Work

In this paper, a new data-driven approach to auto-calibrate the shape sensing functionality of a multi-DOF catheter is presented. The newly presented solution allows the optical fiber to be inserted in an off-center channel while still ensuring a high shape sensing precision. To prove the superiority of the proposed data-driven approach compared to the traditional model-based approach, both methods were implemented in this work. A method to map the curvature measured by the fiber inserted to an off-center channel to the catheter's curvature is also presented. This allows a fair comparison between the two approaches. The performance of the proposed method was evaluated with different ground truths in both free and constrained environments and yielded promising shape sensing accuracy. Using the proposed method, an average shape sensing error of 0.24 mm and 0.49 mm were recorded in free space and constrained space experiments, respectively.

Currently, the training data sets were generated by the catheter tip and base poses with constant curvature assumption. In the future, other sensing modalities such as multi-view 3D computer vision method named shape reconstruction from silhouette [35] will be considered for use in training data generation. The use of shape reconstruction methods from silhouette will enable our method to be also applied to different types of flexible instruments that do not necessary need to follow the constant curvature assumption in free-space during training as was done in this work.

References

[1] T. da Veiga, J. H. Chandler, P. Lloyd, G. Pittiglio, N. J. Wilkinson, A. K. Hoshiar, R. A. Harris, and P. Valdastri, "Challenges of continuum robots in clinical context: A review," *Progress in Biomedical Engineering*, vol. 2, no. 3, p. 032003, 2020.

[2] S. Grazioso, G. Di Gironimo, and B. Siciliano, "A geometrically exact model for soft continuum robots: The finite element deformation space formulation," *Soft robotics*, vol. 6, no. 6, pp. 790–811, 2019.

[3] M. Wagner, S. Schafer, C. Strother, and C. Mistretta, "4d interventional device reconstruction from biplane fluoroscopy," *Medical physics*, vol. 43, no. 3, pp. 1324–1334, 2016.

[4] S. Song, Z. Li, H. Yu, and H. Ren, "Electromagnetic positioning for tip tracking and shape sensing of flexible robots," *IEEE Sensors Journal*, vol. 15, no. 8, pp. 4565–4575, 2015.

[5] J. Avery, M. Runciman, A. Darzi, and G. P. Mylonas, "Shape sensing of variable stiffness soft robots using electrical impedance tomography," in *2019 IEEE International Conference on Robotics and Automation (ICRA)*, 2019, pp. 9066–9072.

[6] G. Gerboni, A. Diodato, G. Ciuti, M. Cianchetti, and A. Menciassi, "Feedback control of soft robot actuators via commercial flex bend sensors," *IEEE/ASME Transactions on Mechatronics*, vol. 22, no. 4, pp. 1881–1888, 2017.

[7] R. Xu, A. Yurkewich, and R. V. Patel, "Curvature, torsion, and force sensing in continuum robots using helically wrapped fbg sensors," *IEEE Robotics and Automation Letters*, vol. 1, no. 2, pp. 1052–1059, 2016.

[8] V. Modes, T. Ortmaier, and J. Burgner-Kahrs, "Shape sensing based on longitudinal strain measurements considering elongation, bending, and twisting," *IEEE Sensors Journal*, vol. 21, no. 5, pp. 6712–6723, 2020.

[9] O. Al-Ahmad, M. Ourak, J. Van Roosbroeck, J. Vlekken, and E. Vander Poorten, "Improved fbg-based shape sensing methods for vascular catheterization treatment," *IEEE Robotics and Automation Letters*, vol. 5, no. 3, pp. 4687–4694, 2020.

[10] C. Culmone, P. W. Henselmans, R. I. van Starkenburg, and P. Breedveld, "Exploring non-assembly 3d printing for novel compliant surgical devices," *Plos one*, vol. 15, no. 5, p. e0232952, 2020.

[11] H. Liu, A. Farvardin, R. Grupp, R. J. Murphy, R. H. Taylor, I. Iordachita, and M. Armand, "Shape tracking of a dexterous continuum manipulator utilizing two large deflection shape sensors," *IEEE sensors journal*, vol. 15, no. 10, pp. 5494–5503, 2015.

[12] A. Farvardin, R. J. Murphy, R. B. Grupp, I. Iordachita, and M. Armand, "Towards real-time shape sensing of continuum manipulators utilizing fiber bragg grating sensors," in *2016 6th IEEE International Conference on Biomedical Robotics and Biomechatronics (BioRob)*. IEEE, 2016, pp. 1180–1185.

[13] X. Li, L. Cao, A. M. H. Tiong, P. T. Phan, and S. J. Phee, "Distal-end force prediction of tendon-sheath mechanisms for flexible endoscopic surgical robots using deep learning," *Mechanism and Machine Theory*, vol. 134, pp. 323–337, 2019.

[14] S. Sefati, C. Gao, I. Iordachita, R. H. Taylor, and M. Armand, "Data-driven shape sensing of a surgical continuum manipulator using an uncalibrated fiber bragg grating sensor," *IEEE Sensors Journal*, 2020.

[15] S. Sefati, R. Hegeman, F. Alambeigi, I. Iordachita, P. Kazanzides, H. Khanuja, R. H. Taylor, and M. Armand, "A surgical robotic system for treatment of pelvic osteolysis using an fbg-equipped continuum manipulator and flexible instruments," *IEEE/ASME Transactions on Mechatronics*, vol. 26, no. 1, pp. 369–380, 2020.

[16] S. Sefati, R. Hegeman, I. Iordachita, R. H. Taylor, and M. Armand, "A dexterous robotic system for autonomous debridement of osteolytic bone lesions in confined spaces: Human cadaver studies," *IEEE Transactions on Robotics*, 2021.

[17] A. Devreker, B. Rosa, A. Desjardins, E. J. Alles, L. C. Garcia-Peraza, E. Maneas, D. Stoyanov, A. L. David, T. Vercauteren, J. Deprest *et al.*, "Fluidic actuation for intra-operative in situ imaging," in *2015 IEEE/RSJ International Conference on Intelligent Robots and Systems (IROS)*. IEEE, 2015, pp. 1415–1421.

[18] J. Legrand, M. Ourak, L. Van Gerven, V. Vander Poorten, and E. Vander Poorten, "A miniature robotic steerable endoscope for maxillary sinus surgery called plient," *Scientific reports*, vol. 12, no. 1, pp. 1–15, 2022.

[19] R. J. Webster III and B. A. Jones, "Design and kinematic modeling of constant curvature continuum robots: A review," *The International Journal of Robotics Research*, vol. 29, no. 13, pp. 1661–1683, 2010.

[20] Z. Zhang, "A flexible new technique for camera calibration," *IEEE Transactions on pattern analysis and machine intelligence*, vol. 22, no. 11, pp. 1330–1334, 2000.

[21] T.-C. Lee, R. L. Kashyap, and C.-N. Chu, "Building skeleton models via 3-d medial surface axis thinning algorithms," *CVGIP: Graphical Models and Image Processing*, vol. 56, no. 6, pp. 462–478, 1994.

[22] P. H. Torr and A. Zisserman, "Mlesac: A new robust estimator with application to estimating image geometry," *Computer vision and image understanding*, vol. 78, no. 1, pp. 138–156, 2000.

[23] X. T. Ha, M. Ourak, O. Al-Ahmad, D. Wu, G. Borghesan, A. Menciassi, and E. Vander Poorten, "Robust catheter tracking by fusing electromagnetic tracking, fiber bragg grating and sparse fluoroscopic images," *IEEE Sensors Journal*, vol. 21, no. 20, pp. 23 422–23 434, 2021.

[24] T. M. Le, B. Fatahi, H. Khabbaz, and W. Sun, "Numerical optimization applying trust-region reflective least squares algorithm with constraints to optimize the non-linear creep parameters of soft soil," *Applied Mathematical Modelling*, vol. 41, pp. 236–256, 2017.

[25] J. J. Moré, "The levenberg-marquardt algorithm: implementation and theory," in *Numerical analysis*. Springer, 1978, pp. 105–116.

[26] T. F. Banchoff and S. T. Lovett, *Differential geometry of curves and surfaces*. CRC Press, 2016.

[27] S. Lim and S. Han, "Helical extension method for solving the natural equation of a space curve," *Surface Topography: Metrology and Properties*, vol. 5, no. 3, p. 035002, 2017.

[28] T. Hastie, R. Tibshirani, and J. Friedman, *The elements of statistical learning: data mining, inference, and prediction*. Springer Science & Business Media, 2009.

[29] G. Cybenko, "Approximation by superpositions of a sigmoidal function," *Mathematics of control, signals and systems*, vol. 2, no. 4, pp. 303–314, 1989.

[30] D. E. Rumelhart, G. E. Hinton, and R. J. Williams, "Learning internal representations by error propagation," California Univ San Diego La Jolla Inst for Cognitive Science, Tech. Rep., 1985.

[31] Y. Zhou, C. Barnes, J. Lu, J. Yang, and H. Li, "On the continuity of rotation representations in neural networks," in *Proceedings of the IEEE/CVF Conference on Computer Vision and Pattern Recognition*, 2019, pp. 5745–5753.

[32] A. Gholamy, V. Kreinovich, and O. Kosheleva, "Why 70/30 or 80/20 relation between training and testing sets: A pedagogical explanation," 2018.

[33] D. Wu, *et al.*, "Hysteresis modeling of robotic catheters based on long short-term memory network for improved environment reconstruction," *IEEE Robotics and Automation Letters*, vol. 6, no. 2, pp. 2106–2113, 2021.

[34] B. K. Horn, "Closed-form solution of absolute orientation using unit quaternions," *Josa a*, vol. 4, no. 4, pp. 629–642, 1987.

[35] S. Baker, T. Kanade *et al.*, "Shape-from-silhouette across time part i: Theory and algorithms," *International Journal of Computer Vision*, vol. 62, no. 3, pp. 221–247, 2005.

Xuan Thao Ha received the M.Sc. degree in systems, control and information technologies from the Université Grenoble Alpes, France, in 2018. He is currently pursuing the dual Ph.D. degrees with the KU Leuven, Belgium, and the Sant'Anna School of Advanced Studies, Italy, with the Marie Skłodowska-Curie ATLAS Project under the European Union Innovative Training Network. He also works with the Robot-Assisted Surgery (RAS) Group, Mechanical Engineering Department, KU Leuven. His research interests include surgical robotic, robot control, and sensing technology.
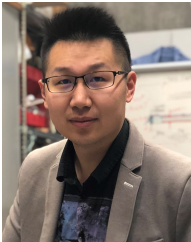
Di Wu (Graduate Student Member, IEEE) received the M.Sc. degree from the Technical University of Munich (TUM), Germany, in 2019. He is currently pursuing dual Ph.D. degrees with the KU Leuven, Belgium, and the Delft University of Technology, the Netherlands, with the Marie Skłodowska-Curie ATLAS Project under the European Union Innovative Training Network. From 2018 to 2019, he was a Visiting Graduate Researcher with the Laboratory for Computational Sensing and Robotics (LCSR), Johns Hopkins University, USA. His first-authored article was awarded the Honorable Mentions of Best Paper Award of IEEE Robotics and Automation Letters in 2021 and finalist of Best Paper Awards IEEE-ISMR in 2019. His research interests include surgical robotics, robot control, and machine learning.

Mouloud Ourak received the M.S. degree in robotics and vision from the Université de Montpellier, France, in 2013, and the Ph.D. degree in automation from the Universit de Franche-Comt in 2016. Since 2017, he has been a Postdoctoral Researcher with the RAS Group, PMA Department, Katholieke Universiteit Leuven, Leuven, Belgium. His research interests include surgical micro-robotics (actuators and control laws) and visual servoing.

Gianni Borghesan received an M.S. degree from the University of Pisa in 2004, and a Ph.D. degree from the University of Bologna in 2008. From 2008 to 2010, he was a Postdoctoral Researcher at the University of Bologna. Since 2010, he has been working with the Department of Mechanical Engineering, KU Leuven, participating in several research projects in the field of Robotics. He is currently a Research Expert with the Department of Mechanical Engineering and Core Lab ROB, Flanders Make of KU Leuven. His research interests include constraint-based control, teleoperation and haptics, and robotic surgery.

Jenny Dankelman received the M.Sc. degree in mathematics in 1984, with a specialization in system and control engineering at the University of Groningen, Groningen, The Netherlands and the Ph.D. degree in dynamics of the coronary circulation from the Man-Machine Systems Group, Delft University of Technology, Delft, The Netherlands, in 1989.,She continued her research at the Man-Machine Systems group and in 2001 she became a Professor in minimally invasive technology. In 2007, she became the Head of the Minimally Invasive Surgery and Interventional Techniques Group. She is cooperating with surgeons of several (university) hospitals, e.g., Leiden University Medical Center, Erasmus Medical Center Rotterdam, Reinier de Graaf Hospital Delft, Academic Medical Center Amsterdam. Her research interests include designing novel medical instruments, medical haptics, training and simulation, and patient safety, with the focus on minimally invasive techniques.

Arianna Menciassi (Senior Member, IEEE) received the M.Sc. degree in physics from the University of Pisa, Pisa, Italy, in 1995, and the Ph.D. degree in bioengineering from Scuola Superiore Sant'Anna, Pisa, in 1999. She is currently a Professor of Bioengineering and Biomedical Robotics with the Scuola Superiore Sant'Anna, where she is the Team Leader of Surgical Robotics and Allied Technologies with the BioRobotics Institute. She has been the Coordinator of the Ph.D. in BioRobotics since 2018, and she was appointed in 2019 as the Vice-Rector of the Scuola Superiore Sant'Anna. Her research interests include surgical robotics, microrobotics for biomedical applications, biomechatronic artificial organs, and smart and soft solutions for biomedical devices. She pays a special attention to the combination between traditional robotics, targeted therapy, and wireless solution for therapy (e.g., ultrasound- and magnetic-based solutions). Prof. Menciassi is the Co-Chair of the IEEE Technical Committee on Surgical Robotics. She was in the Editorial Board of the IEEE-ASME Transactions on Mechatronics from 2009 to 2013. She was a Topic Editor of the International Journal of Advanced Robotic Systems from 2013 to 2020. She is currently an Editor of the IEEE Transactions on Robotics and APL Bioengineering. She is an Associate Editor of the IEEE Transactions on Medical Robotics and Bionics and the Soft Robotics journal.

Emmanuel Vander Poorten received the Ph.D. degree from Kyoto University, Japan, in 2007. He is currently an Associate Professor with the Mechanical Engineering Department, KU Leuven, Belgium. He is the Co-ordinator of the Robot-Assisted Surgery Group, the Founder of CRAS, the Joint Conference on New Technologies for Computer/Robot Assisted Surgery and Steering Board Member of ACTU-ATOR a biennial event bringing together leading experts, suppliers and users of new actuators and low-power electromagnetic drives. He is active in international collaborative research projects, participating, and co-ordinating several EU-funded projects on medical robotics. His research interests include medical device design, robotic co-manipulation, haptics, teleoperation, control of flexible instruments, and robotic catheters.